

Fluid Flow Modeling of a Gas-induced Pulsating Flow Bubble Column

X. Jia,^{a,b} Q. Yuan,^a J. Wen,^{a,b,*} and W. Feng^a

^aDepartment of Biochemical Engineering, School of Chemical Engineering and Technology, Tianjin University, Tianjin 300072, P. R. China

^bKey Laboratory of Systems Bioengineering (Tianjin University), Ministry of Education, Tianjin 300072, P. R. China

Original scientific paper

Received: July 19, 2010

Accepted: February 14, 2011

A three-dimensional (3D) Euler-Euler gas-liquid two-phase mathematical model was developed for simulating the local transient fluid flow in a gas-induced pulsating flow bubble column using computational fluid dynamic (CFD) method, with multiple size group (MUSIG) model implemented to predict the bubble size distribution. Model simulated results such as local transient axial liquid velocities and time-averaged liquid turbulent kinetic energy distributions were validated successfully by corresponding experimental measurements under varied operating conditions, i.e. pulsating amplitudes and frequencies. It was found that the liquid turbulent kinetic energy increased with the increase in pulsating amplitude and frequency, and a maximum value appeared at an axial position of $Z = 0.4$ m, centerline of the column. Furthermore, local transient fluid flow characters such as the gas holdups, gas velocity fields and liquid velocity fields, as well as bubble size distributions were predicted reasonably by the proposed model.

Key words:

Bubble column, gas-induced pulsating flow, fluid flow, bubble size distribution, CFD, MUSIG model

Introduction

It is well known that superimposing fluid pulse in a reactor can improve fluid mechanical conditions and alter flow patterns within the device, and consequently, achieve an enhanced phase mixing, which then leads to an improved mass and heat transfer performance.^{1–3} Thus the pulsating flow would have good potential in applications in chemical and biochemical industries such as oxidation and hydrogenation reactions, fine chemical productions, pharmaceutical synthesis, VOCs (volatile organic compounds) and wastewater treatments, and so forth.

The oscillatory baffled reactor is a newly developed mixing device and has been studied in gas-liquid systems based on the methodology of superimposing periodic fluid oscillations onto a cylindrical column containing evenly spaced orifice baffles.^{2,4} Fluid oscillation was achieved by means of a piston or bellows at the base of the column, or by moving a set of baffles up and down. It was found that the volumetric mass transfer coefficients $k_L a$ in the pulsating baffled reactor were much higher than those obtained under the steady state. Knopf *et al.*³ studied bubble properties as well as mass transfer coefficients in a pulsating bubble column at low amplitudes and modest frequencies (0–30 Hz). Krishna and Ellenberger⁵ applied low frequency

vibration to the liquid phase of an air-water bubble column with a louder speaker, where improvement of $k_L a$ was achieved by 30–100 %, depending on the operating gas velocities. Godó *et al.*⁶ investigated periodical change of input air flow rate with a cycle of 15–30 min in an airlift bioreactor during citric acid fermentation. They found that when keeping the reactor in an unsteady state, it was operated more efficiently with increased dissolved oxygen even with high viscous fermentation broth.

All of the above studies are focused on the macroscopic view of the effect of pulse on reactor performance, such as mass transfer and/or gas bubble properties. Because of the lack of advanced measuring technologies, it is difficult to know the local, transient and microscopic hydrodynamics in a more detailed mode, resulting in very scarce literature in this field. However, understanding these characteristics is of great importance in reactor optimal design, operation, and scale-up.

In recent years, the computational fluid dynamic (CFD) method has become a widely accepted technique for multi-phase process simulation, which provides a detailed prediction and understanding of the hydrodynamics, to the benefit of design and optimization of bubble columns and other reactors. However, as far as we know, it has not yet been applied to the gas-induced pulsating flow bubble column.

*Corresponding author. E-mail: jpwen@tju.edu.cn

Table 1 – Bubble group diameter discretization in the simulation

Bubble group i	1	2	3	4	5	6	7	8	9	10
Bubble diameter/mm	1.7	3.1	4.5	5.9	7.3	8.7	10.1	11.5	12.9	14.3

air flow. The pulsating “on” time t_p (opening state) and the pulsating “off” time t_b (close state) were set to be equal to $T/2$. In this mode, a square-wave cycled pulsating gas feeding was achieved. The pulsating cycles were set as 0.2, 0.4 and 0.8 s, corresponding to the pulsating frequencies of 5, 2.5 and 1.25 Hz, respectively.

Local liquid velocity measurement

Quantitative liquid velocity measurement was performed with a Dantec three-dimensional laser Doppler Anemometer (LDA) working in the backward scattering mode. Laser light was provided by a 5 W water-cooled Argon-ion laser and a beam separator was used to generate three pairs of laser beams with wavelengths of 476, 488 and 514.5 nm respectively, in order to measure the three velocity components simultaneously. More details can be found in a previously published paper in our lab.¹⁰ All the experiments were repeated three times while the data shown in corresponding figures were the averaged ones. Relative standard deviations of the experimental data were all within $\pm 3\%$.

Numerical simulation setup and procedure

In the present study, the unsteady flow in the gas-induced pulsating flow bubble column was modeled using a full-dimensional Euler-Euler gas-liquid two-phase CFD model. MUSIG model was implemented to take into consideration of the non-uniform bubble size distribution including bubble coalescence and break-up effects. Bubbles with diameter ranging from 1 to 15 mm observed in the experiments under the investigated operating conditions were divided into 10 groups based on the equal diameter discretization method (Table 1). Instead of considering 10 different phases separately, all the bubble groups were assumed to move at the same mean velocity.^{7,11} Therefore, 1 momentum and 10 continuity equations were to be solved for the gas phase while 1 momentum and 1 continuity equation for the liquid phase.

Governing equations

In the Euler-Euler two-phase CFD model, mass and momentum balance equations are solved for each phase, and were given as follows:

$$\frac{\partial(\varepsilon_l \rho_l)}{\partial t} + \nabla \cdot (\varepsilon_l \rho_l \mathbf{u}_l) = 0 \quad (1)$$

$$\frac{\partial(\varepsilon_g \rho_g f_i)}{\partial t} + \nabla \cdot (\varepsilon_g \rho_g \mathbf{u}_g f_i) = S_i \quad (2)$$

$$\begin{aligned} & \frac{\partial(\varepsilon_g \rho_g \mathbf{u}_g)}{\partial t} + \nabla \cdot (\varepsilon_g (\rho_g \mathbf{u}_g \mathbf{u}_g)) = \\ & = -\varepsilon_g \nabla p + \nabla \cdot (\varepsilon_g \mu_{eff,g} (\nabla \mathbf{u}_g + (\nabla \mathbf{u}_g)^T)) + \\ & \quad + \varepsilon_g \rho_g \mathbf{g} - \mathbf{M}_l \end{aligned} \quad (3)$$

$$\begin{aligned} & \frac{\partial(\varepsilon_l \rho_l \mathbf{u}_l)}{\partial t} + \nabla \cdot (\varepsilon_l (\rho_l \mathbf{u}_l \mathbf{u}_l)) = \\ & = -\varepsilon_l \nabla p + \nabla \cdot (\varepsilon_l \mu_{eff,l} (\nabla \mathbf{u}_l + (\nabla \mathbf{u}_l)^T)) + \\ & \quad + \varepsilon_l \rho_l \mathbf{g} + \mathbf{M}_l \end{aligned} \quad (4)$$

where ε_g and ε_l , the gas phase and liquid phase volume fractions, are related by the following summation constraint:

$$\varepsilon_g + \varepsilon_l = 1 \quad (5)$$

and in eq. (2), S_i is the source term due to bubble break-up and coalescence of the i th bubble group ($i = 1, \dots, 10$); f_i is defined as the size fraction of the i th bubble group, which has a relationship with the gas holdup as follows:

$$n_i V_i = \varepsilon_g f_i \quad (6)$$

where n_i is the number density of the i th bubble group, and V_i is the volume of the i th bubble group. The bubble Sauter mean diameter based on the calculated values of the scalar fraction f_i and discrete bubble size d_i can be calculated from the following equation:

$$\frac{1}{d_s} = \sum_i \frac{f_i}{d_i} \quad (7)$$

Bubble break-up and coalescence models

In bubble columns, the initial bubble size is determined by its formation at the distribution plate. However, these initial bubbles may not be stable due to turbulence, interfacial instability and wake entrainment as the flow develops in the column. In all cases, the bubble size is further determined by a break-up and coalescence mechanism. In order to

predict the bubble size distribution in a gas-liquid flow, population balance equations (PBEs) can be used.^{12–14} At the right side of eq. (2), the source term S_i for the i th bubble group is given by:

$$S_i = B_{break-up} - D_{break-up} + B_{coalescence} - D_{coalescence} \quad (8)$$

where the last four terms of this equation represent the birth rate B and death rate D due to break-up and coalescence. The bubble break-up and bubble coalescence kernels have been provided in detail in a previously published paper of our lab,¹⁵ and the case is the same for the interface force and turbulence closure models,¹⁰ thus they were not repeated here.

Boundary conditions

The boundary conditions at the inlet were defined as follows:

$$\begin{cases} u_{g,inlet,z} = Q_{g,inlet}(t)/S_{inlet} \\ u_{g,x} = u_{g,y} = 0 \\ u_{l,x} = u_{l,y} = u_{l,z} = 0 \\ \varepsilon_g = 1, \quad \varepsilon_l = 0 \end{cases} \quad (9)$$

$Q_{g,inlet}(t)$ is the gas volumetric flow rate which varies with time t in a form of square wave as shown in Fig. 1b. Under the condition of the unsteady operation, $Q_{g,inlet}(t)$ is described as:

$$Q_{g,inlet}(t) = Q_b + Q_p \cdot \text{step}(\sin(2\pi f \cdot t)) \quad (10)$$

where Q_b and Q_p are the volumetric flow rates of the base flow and pulsating flow, respectively; f is the pulsating frequency; the *step* function is defined as follows:

$$\text{step}(\theta) = \begin{cases} 1 & \text{for } \theta \geq 0 \\ 0 & \text{for } \theta < 0 \end{cases} \quad (11)$$

In this study, a constant base flow rate of $0.18 \text{ m}^3 \text{ h}^{-1}$ was used to make flow normally fluidized while minimizing the effect of the base flow as much as possible. The pulsating flow rates were set to be 1.37, 1.94 and $2.52 \text{ m}^3 \text{ h}^{-1}$. Superficial gas velocities (defined as $u_g = (Q_b + 0.5Q_p)/S_{BC}$) representing the pulsating amplitude were 0.006, 0.008 and 0.01 m s^{-1} , correspondingly.

Bubble diameter at the distribution plate is assumed to be uniform and was calculated by the correlation presented by Miyahara *et al.*¹⁶ As $d_o^{1.5} u_{g,inlet} \rho_l \mathbf{g}^{0.5} / \sigma \leq 1$ in this study (where d_o is the diameter of the orifice and $u_{g,inlet}$ is the superficial gas velocity at the distribution plate), the size of

bubbles produced at the orifice $d_{B,O}$ is calculated by:

$$d_{B,O} = 2.9 \left(\frac{\sigma d_o}{\rho_l \mathbf{g}} \right)^{\frac{1}{3}} \quad (12)$$

Along the walls, no-slip boundary was applied for the liquid phase, while free-slip boundary was used for the gas phase. At the outlet of the column, a degassing boundary was defined, which allows only the gas phase to escape.¹⁰

Numerical implement

In order to numerically solve the system of partial and ordinary differential equations presented above, “High-Resolution” discretization of the equations was carried out using a finite volume scheme with a coupled multigrid solver as implemented in the CFD code CFX-5.6. A full-implicit scheme technology was used by solving the full hydrodynamic system of equations simultaneously across all grid nodes. An unstructured numerical grid has been implemented with an average grid size of $10 \times 10 \times 20 \text{ mm}$, corresponding to a total number of 12 000 cells. To save computing time, a time-stepping strategy was used in the transient simulations based on the suggestion of Krishna *et al.*¹⁷ $400 \times 0.005 \text{ s}$, $1000 \times 0.01 \text{ s}$, $1000 \times 0.02 \text{ s}$, $1000 \times 0.05 \text{ s}$, and for the rest time of total 150 s a time step length of 0.1 s was used. A RMS convergent goal of $1 \cdot 10^{-4}$ was specified for all variables calculated in this study.

Results and discussion

Effect of operating conditions

It is known that turbulence plays a very important role in multiphase mass transfer, heat transfer and phase mixing. Turbulent kinetic energy k of the liquid phase can be calculated from the following equation:¹⁸

$$k = \frac{1}{2} (\langle uu \rangle + \langle vv \rangle + \langle ww \rangle) \quad (13)$$

$$\langle u_i u_i \rangle = \frac{1}{N} \sum_{j=1}^N (u_i(j) - \bar{u}_i)^2 \quad (14)$$

$$\bar{u}_i = \frac{1}{N} \sum_{j=1}^N u_i(j) \quad (15)$$

where u_i represents the liquid velocity components u , v and w , respectively; $u_i(j)$ is the local transient liquid velocity components at time j ; and N is the

total number of samples in the sampling period. The results from LDA measurements are time series of transient velocity of the liquid phase. It allows measuring all of the three components (X - Y - Z) of the liquid velocity simultaneously at one point. Thus, it is possible to use liquid turbulent kinetic energy for the characterization of the turbulence properties in this gas-induced pulsating flow bubble column.

Effects of pulsating amplitude

Fig. 2a shows the effect of pulsating amplitude, represented by superficial gas velocity u_g , on the time-averaged turbulent kinetic energy k at pulsating frequency of 1.25 Hz and axial position $Z = 0.4$ m. It can be seen from the figure that the turbulent kinetic energy radial distribution profiles are parabolic and the peak values appear in the central regime of the bubble column, where the rising bubbles and bubble wakes pass through. It is also noted that the turbulent kinetic energy increases with the increase in superficial gas velocity. Similar results can be found in Cui and Fan's¹⁸ study under the bubbly flow at low superficial gas velocities.

Effect of pulsating frequency

The local time-averaged turbulent kinetic energy is also affected by the pulsating frequency as can be noted from Fig. 2b. It indicated that the turbulent kinetic energy increases with the increase in pulsating frequency under superficial gas velocity of 0.01 m s^{-1} . This is mainly due to the faster periodical alternation of the gas feeding on and off states under higher pulsating frequency, which introduces more intensive turbulence on the liquid phase. However, it is worth noting that the turbulent kinetic energy at pulsating frequency $f = 1.25$ Hz is a little lower than that obtained under the steady state. This may be attributed to the higher energy dissipation at lower pulsating frequency with longer time interval between the feeding on and off states.

Effect of axial position

A typical result of the local time-averaged turbulent kinetic energy as a function of the axial position at the same pulsating amplitude and frequency is shown in Fig. 2c. It implies that the liquid phase is accelerated by the rising bubbles. Turbulent kinetic energy increases with the increase in axial position at lower part of the bubble column where fluid flow develops. However, at upper part of the column, where gas-liquid phase separation takes place, the turbulent kinetic energy decreases, and the distribution profile becomes flatter, which is

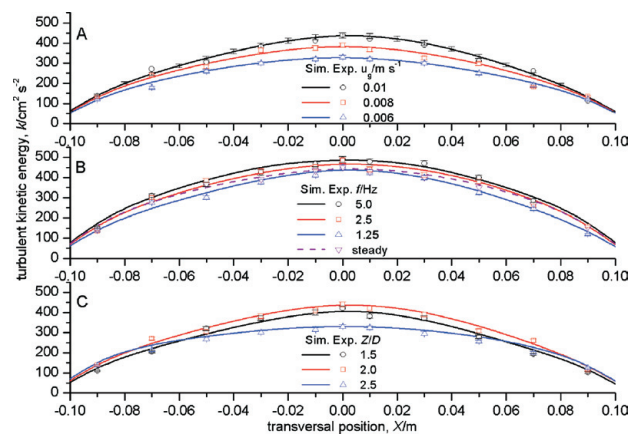


Fig. 2 – Effect of a: pulsating amplitude ($f = 1.25$ Hz and $Z/D = 2.0$), b: pulsating frequency ($u_g = 0.01 \text{ m s}^{-1}$ and $Z/D = 2.0$), c: dimensionless axial position ($u_g = 0.01 \text{ m s}^{-1}$ and $f = 1.25$ Hz) on the local time-averaged liquid turbulent kinetic energy

mainly attributed to the momentum transfer and energy dissipation in the liquid phase. Hence a maximum turbulent kinetic energy appears at the centerline of the column at an axial position of $Z = 0.4$ m, or $Z/D = 2$.

Quantitative comparison between experiment and simulation

Quantitative comparison between the experimental and simulated local time-averaged liquid turbulent kinetic energy of the gas-induced pulsating flow bubble column are also presented in Fig. 2. It is clearly shown that the simulated values are in reasonable agreement with the corresponding data from LDA experiment. However, the above analysis does not represent the transient turbulent structure of the flow which plays an important role in multiphase system performance. Therefore, it is of great importance to make a comparison of the transient flow behavior between the experimental data and the simulated results.

Fig. 3 shows the time-dependent fluid flow of the axial liquid velocity under varied operating conditions. It is noted that the velocity fluctuation consists of a low-frequency part induced by the bubble swarm wagging and a high-frequency part caused by the pulsating gas feeding. The quantitative comparison of the experimental data and the simulated results was carried out at a certain point ($X = 0$ m, $Y = 0$ m, $Z = 0.4$ m). A Fast Fourier Transformation (FFT) was applied to the experimental time series data in order to separate the relative low-frequency part caused by the bubble swarm wagging and gas pulsating from the extremely high-frequency fluctuation caused by phase turbulence.

The liquid velocity fluctuation caused by the pulsating gas feeding is clearly represented in the

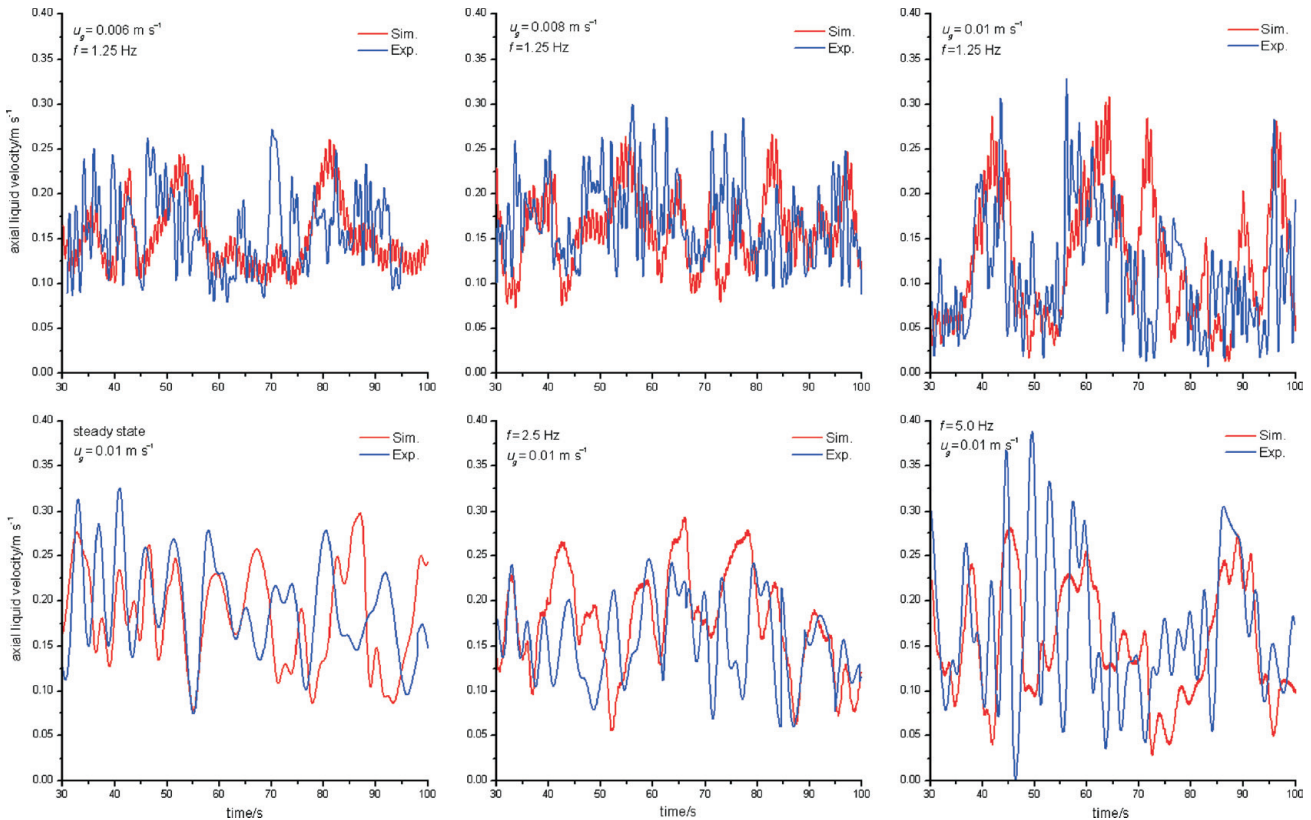


Fig. 3 – Local transient liquid velocity comparison of FFT-filtered experimental data and simulation results at a certain position ($X = 0$ m, $Y = 0$ m, $Z = 0.4$ m) under different superficial gas velocities ($f = 1.25$ Hz) and pulsating frequency ($u_g = 0.01$ m s⁻¹)

upper part of Fig. 3. It is shown that the fluctuation amplitude increases with the increase in superficial gas velocity; while for the low-frequency part caused by the bubble swarm wagging, it also increases. Especially, for $u_g = 0.006$ m s⁻¹, flow is more uniform with flatter velocity distribution profile and fewer large peaks. When operating under different pulsating frequency at the same superficial gas velocity as shown in the lower part of Fig. 3, the low-frequency fluctuations caused by the bubble swarm wagging appear to have similar shapes with each other. However, the high-frequency fluctuations caused by the pulsating gas feeding seem to be attenuated by the faster “on and off” alternation with the increase in pulsating frequency.

It is noted that there is some difference between the experimental data and the simulation results, the reasons are as follows: 1) the transient velocity fluctuation is greatly influenced by the bubble swarm wagging, which is rather random in the bubble column, so it is difficult for the peaks to appear at the same time in the two curves; 2) the high-frequency fluctuation in the simulated curve is caused by the pulsating gas feeding, while the LDA results are not only influenced by operating conditions, but also sampling frequency of the equip-

ment; FFT may also introduce some errors during the process.

Nevertheless, some parts of the two curves agree very well as can be seen from the figure, and the values are almost in the same magnitude. Generally speaking, the modeling results of the local time-averaged turbulence properties and transient flow behaviors both show reasonable good agreement with the experimental data.

Bubble properties

Local transient bubble size distribution snapshots at $t = 60$ s under $u_g = 0.01$ m s⁻¹ and $f = 1.25$ Hz are represented in Fig. 4. It is shown that bubbles with diameters smaller than 8.7 mm (group 6) mainly occupy the whole bubble column. As group 3 ($d_3 = 4.5$ mm) contains the initial bubbles from the distribution plate, its volume fraction is the largest and it mainly occupies the bottom of the column. It breaks up and coalesces when rising in the column, and many new smaller or larger bubbles form as a result. As can be concluded from the snapshots, coalescence is the main effect of the bubble reaction. The volume fraction of smaller bubbles ($d < 4.5$ mm) is relatively small and they mainly occupy the near-wall and upper section of

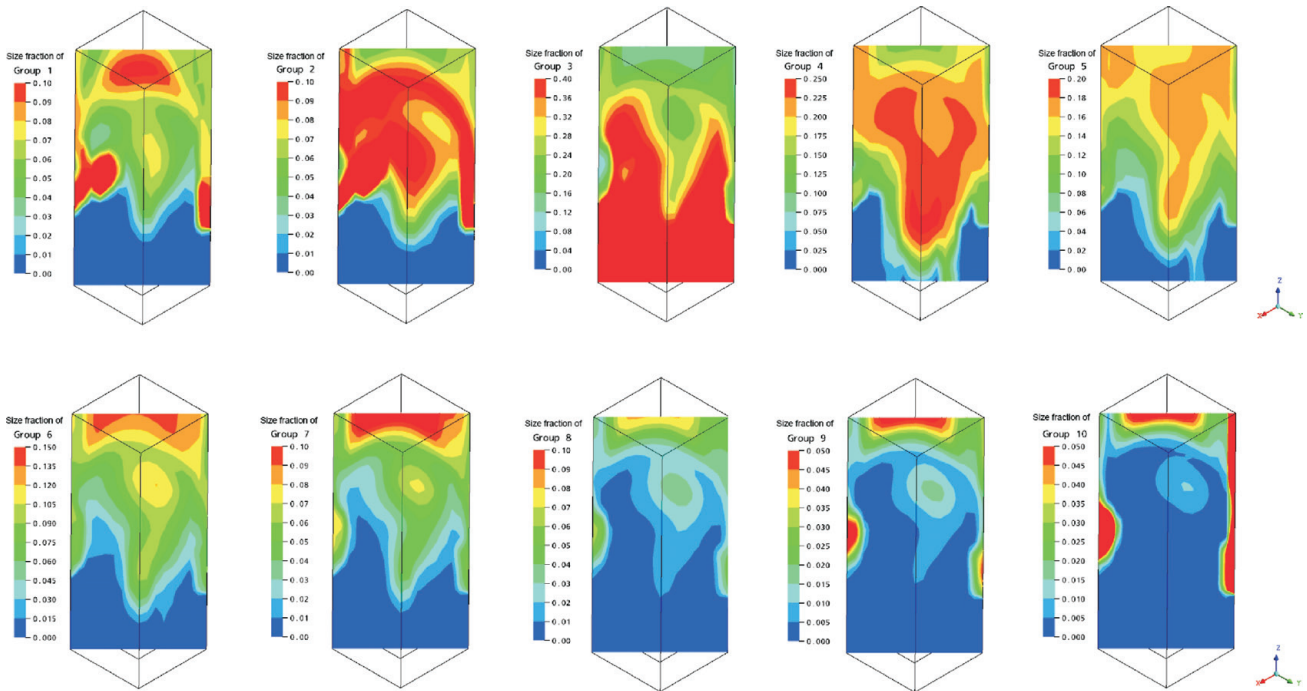


Fig. 4 – Local transient bubble size distribution snapshots ($t = 60$ s, $u_g = 0.01$ m s⁻¹ and $f = 1.25$ Hz)

the column. Most of them are brought back to the bottom by the liquid recirculation. The larger bubbles ($d > 4.5$ mm), however, are mainly concentrated at the center of the bubble column, especially for group 4 ($d_4 = 5.9$ mm) and group 5 ($d_5 = 7.3$ mm).

The time- and column volume-averaged bubble size distributions under different operating conditions are shown in Fig. 5. For different pulsating amplitude of u_g at a constant pulsating frequency of $f = 1.25$ Hz, the bubble size distribution profiles become sharper and narrower with the decrease in u_g . While for the increase in pulsating frequency with u_g being equal to 0.01 m s⁻¹, the distribution profiles tend to broaden significantly and two peaks appear for a higher frequency of 5 Hz. Krishna and Ellenberger⁵ reported that the churn-turbulent flow could be characterized by a bimodal bubble size distribution. Thus it indicates that a transition from homogeneous bubbly flow regime to churn-turbulent flow regime occurs under the high intensive pulsating state with $f = 5$ Hz. This flow pattern transition could also be observed during the experiment. Therefore it can be concluded that the imposed pulse can lead to an extension of churn-turbulent flow regime even under relatively low gas velocities.

Model prediction

It is very important and necessary for the applied CFD model to be used for the prediction of the local transient flow behaviors of the square

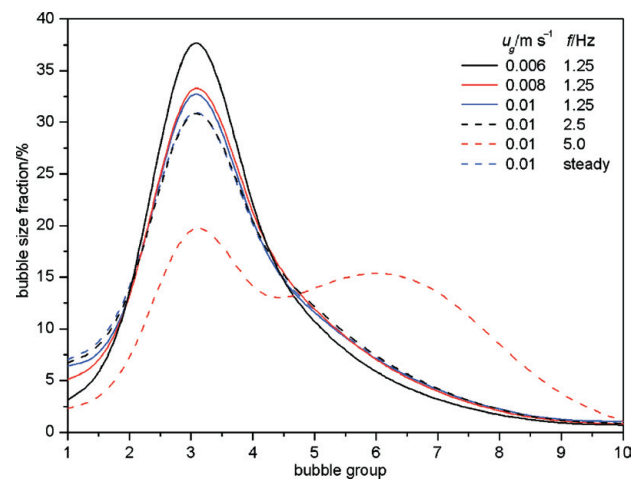


Fig. 5 – Time- and volume-averaged bubble size distributions under different operating conditions

cross-sectional two-phase gas-induced pulsating flow bubble column. Snapshots of the gas holdups, gas velocity fields and liquid velocity fields at $t = 30.0, 30.4, 30.8$ and 100 s are shown in Fig. 6a-c, respectively. It can be seen that flow was driven by both the periodical gas pulse and bubble swarm wagging through the column in an oscillatory manner. Large vortices alongside the bubble swarm are induced not only in liquid velocity fields but also in gas velocity fields; it is also worth noting that there are usually two vortices in the former one. Many small bubbles were carried downward to the bottom of the column by liquid recirculation.

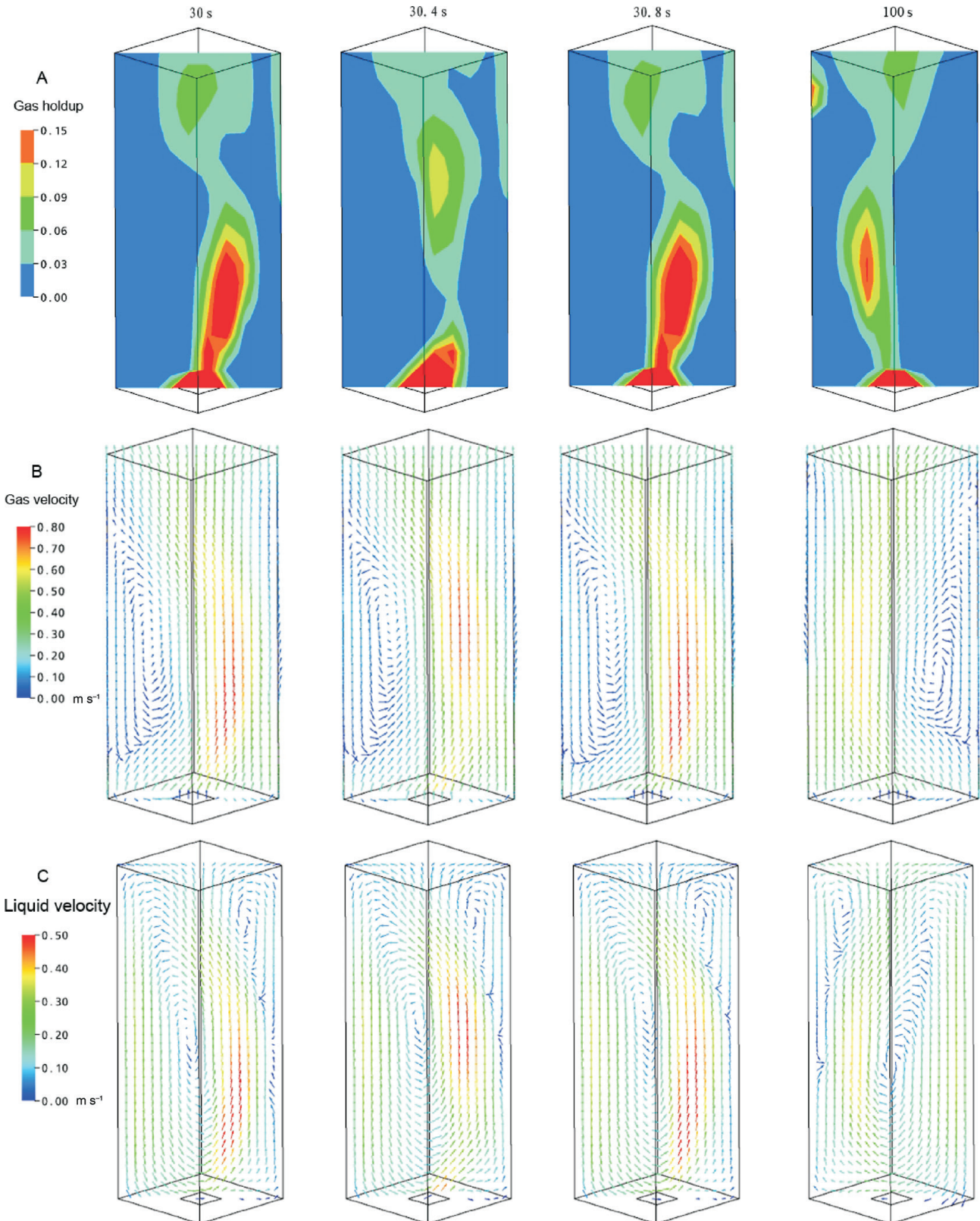


Fig. 6 – Model prediction of a: gas holdups, b: gas velocity fields, c: liquid velocity fields at $t = 30, 30.4, 30.8$ and 100 s, respectively ($u_g = 0.008$ m s⁻¹, and $f = 1.25$ Hz)

Conclusion

In this study, a three-dimensional CFD model for prediction of flow patterns in the gas-induced pulsating flow bubble column is developed. In parallel, experimental investigation of a gas-induced pulsating flow has been performed in a square cross-sectional bubble column. The local hydrodynamic performance such as the transient axial liquid velocity and the turbulent structure characterized by the liquid turbulent kinetic energy were measured and simulated systematically with different pulsating amplitude represented by superficial gas velocity and pulsating frequency. The model is quantitatively validated by the experimental data of the measured turbulent kinetic energy and the transient axial liquid velocity. The results show that the turbulent kinetic energy increased with the increasing in pulsating amplitude and frequency, and a maximum value appeared at the centerline with $Z/D = 2$ of the column. Based on the validated CFD modeling approach, the bubble size distributions under different operating conditions were uncovered which provides the important evidence that imposed pulsating may lead to extension of churn-turbulent flow regime even at relatively low gas velocity. In addition, the transient flow structures, such as the gas holdups, gas velocity fields and liquid velocity fields, were predicted by this model, which would provide a direct view on the flow performance as well as important information on strategies of operation optimization, reactor design and scale up process of the gas-induced pulsating flow bubble column.

ACKNOWLEDGEMENTS

The authors wish to acknowledge the financial support provided by the National 973 Project of China (No. 2007CB714302) and the National Natural Science Foundation of China (No. 20976124 and No. 20906070).

Nomenclature

B	– birth source, $\text{kg m}^{-3} \text{ s}^{-1}$
D	– death source, $\text{kg m}^{-3} \text{ s}^{-1}$, in eq. (8)
D	– diameter of the column, m
D	– diameter, m
d_S	– bubble Sauter mean diameter, m
F	– pulsating frequency, Hz
f_i	– i th bubble group size fraction, dimensionless
G	– gravitational acceleration, 9.81 m s^{-2}
k	– turbulent kinetic energy, $\text{cm}^2 \text{ s}^{-2}$
M_I	– interface force between the gas phase and suspension phase, N m^{-3}

n	– number density, m^{-3}
p	– pressure, Pa
Q	– volumetric flow rate, $\text{m}^3 \text{ s}^{-1}$
S	– source term, $\text{kg m}^{-3} \text{ s}^{-1}$
S_{inlet}	– area of gas inlet, m^2
T	– pulsating cycle, s
t	– time, s
t_b	– pulsating “off” time, s
t_p	– pulsating “on” time, s
u_g	– superficial gas velocity, m s^{-1}
\mathbf{u}	– velocity vector, m s^{-1}
u	– velocity at X -direction, m s^{-1}
V	– volume, m^3
v	– velocity at Y -direction, m s^{-1}
w	– velocity at Z -direction, m s^{-1}
X, x	– X -direction position, m
Y, y	– Y -direction position, m
Z, z	– Z -direction (axial) position, m

Greek letters

ε	– volume fraction, dimensionless
μ	– viscosity, $\text{Pa} \cdot \text{s}$
ρ	– density, kg m^{-3}
σ	– surface tension, N m^{-1}

Subscripts

B	– bubble
BC	– bubble column
b	– base flow
eff	– effective
g	– gas phase
i	– i th bubble group
$inlet$	– gas inlet
l	– liquid phase
o	– orifice
p	– pulsating flow
t	– time
x	– X -direction
y	– Y -direction
z	– Z -direction

References

1. Silveston, P. L., *Sadhana-Academy Proceedings in Engineering Sciences* **10** (1987) 217.
2. Ni, X., Gao, S., *J. Chem. Technol. Biot.* **65** (1996) 65.
3. Knopf, F. C., Ma, J., Rice, R. G., *AIChE J.* **52** (2006) 1103.
4. Oliveira, M. S. N., Ni, X., *Chem. Eng. Sci.* **56** (2001) 6143.
5. Krishna, R., Ellenberger, J., *Chem. Eng. Technol.* **20** (2002) 159.

6. *Godó, Š., Klein, J., Polakovic, M., Bálaš, V.*, Chem. Eng. Sci. **54** (1999) 4937.
7. *Olmos, E., Gentric, C., Vial, C., Wild, G., Midoux, N.*, Chem. Eng. Sci. **56** (2001) 6359.
8. *Yeoh, G. H., Tu, J. Y.*, Chem. Eng. Sci. **56** (2004) 3125.
9. *Yeoh, G. H., Tu, J. Y.*, AIChE J. **51** (2005) 8.
10. *Feng, W., Wen, J. P., Fan, J. H., Yuan, Q., Jia, X. Q., Sun, Y.*, Chem. Eng. Sci. **60** (2005) 6887.
11. *Chen, P., Sanyal, J., Duduković, M. P.*, Chem. Eng. Sci. **60** (2005) 1085.
12. *Bannari, R., Kerdouss, F., Selma, B.*, Comput. Chem. Eng. **32** (2008) 3224.
13. *Miura, M., Vinogradov, O.*, Comput. Chem. Eng. **32** (2008) 1249.
14. *Silva, L. F. L. R., Damian, R. B., Lage, P. L. C.*, Comput. Chem. Eng. **32** (2008) 2933.
15. *Jia, X. Q., Wen, J. P., Zhou, H. L., Feng, W., Yuan, Q.*, AIChE J. **53** (2007) 2221.
16. *Miyahara, T., Matsuba, Y., Takahashi, T.*, Int. Chem. Eng. **23** (1983) 517.
17. *Krishna, R., van Baten, J. M., Urseanu, M. I., Ellenberger, J.*, Chem. Eng. Sci. **56** (2001) 537.
18. *Cui, Z., Fan, L. S.*, Chem. Eng. Sci. **59** (2004) 1755.